PORE-SCALE NUMERICAL INVESTIGATION ON COMPREHENSIVE HEAT TRANSFER PERFORMANCE OF HOMOGENEOUS AND GRADED METAL FOAM HEAT SINKS BASED ON TETRAKAIDECAHEDRON CELL

Hangming SHEN[1], Chao LIU[1], Lihong YANG[1 *] , Yuanli WANG[2]

[*1] School of Mechanical Engineering, University of Shanghai for Science and Technology, Shanghai, China

[2] Shanghai Lingwo Electronic Technologies Co., Ltd, Shanghai, China

[*] Corresponding author; E-mail: lhyang@usst.edu.cn

In order to improve the heat dissipation efficiency of heat sinks, heat sinks filled with metal foam were proposed and numerically studied in this work. Different shapes, including the tetrakaidecahedron, triangular prism, and equivalent tetrahedron, were employed to develop geometries for the cells, ligaments, and nodes of the metal foam. Computational simulation was carried out to analyze the hydraulic and thermal performance of the homogeneous metal foam (HMF)-filled heat sinks and graded metal foam (GMF)-filled heat sinks. The study found that well-designed GMF-filled heat sinks can improve both hydraulic and thermal performance. A graded PPI negative change along the X-axis direction can improve the comprehensive heat transfer performance (CHTP), and the positive change has a similar effect. Graded PPI negative change along the Y-axis direction can effectively improve the CHTP, while the positive change has no effect. Moreover, a greater thickness of the metal foam with a larger PPI leads to better performance. GMF-filled heat sinks can also effectively reduce the surface temperature of the bottom plane and enhance the convection performance.

Key words*: Graded metal foam, Tetrakaidecahedron, Comprehensive heat transfer performance, Heat sink, Heat dissipation*

1. Introduction

Efficient heat dissipation of electronic components is the key technology to ensuring its service life and stable operation. Heat dissipation techniques for electronic components vary widely based on equipment layout and needs, such as air-forced convection cooling[1], liquid cooling[2], heat pipe cooling[3, 4], etc. Among existing methods, heat sinks are widely used due to their advantages of low cost, high heat transfer efficiency, and good reliability[5]. The efficiency of heat sink in dissipating performance depends on many factors, such as the heat transfer area, heat transfer coefficient, heat conduction, and flow resistance characteristics, etc., and largely depends on the structure of the heat

transfer medium. Therefore, in general, heat sinks can be divided into solid fin systems[6, 7], microchannel systems[8, 9], and filled porous materials[10-12], etc.

Porous medium can be widely used in the field of heat transfer [13-17]. Metal foam is a type of porous material that offers several advantages, such as a large specific surface area, high thermal conductivity, lightweight construction, and excellent heat transfer performance. Electronic devices with heat sinks should be small and light, which require a higher surface area for effective heat dissipation. Because of these characteristics, extension surface used in heat sinks is challenging to achieve. Therefore, metal foam-filled heat sinks have become a popular research topic in late years. Generally, the primary objective of the structure design for metal foam-filled heat sinks is to increase the contact surface area between the metal foam and the cooling medium while minimizing the pressure drop so as to ensure that the entire cooling cycle can be performed continuously at a low cost. Sandwich-like heat sinks can be formed by placing high-porosity, open-cell copper foam blocks between fins to increase the heat transfer surface area [18]. Also, the optimized micro-channel heat sinks were designed by attaching various metal foams to copper plates [19]. Furthermore, the thermal resistance enhancement of an innovative heat sink both with nanocoated and uncoated metallic foams were experimentally investigated [20]. As already seen, metal foam-filled heat sinks offer a substantial increase in thermal performance. However, this comes at the expence of high-pressure drop and pumping power. Hence, one potential approach to enhance heat transfer and minimize flow resistance is to use non-uniform metal foam configurations. In addition, numerical simulation attempts have been made in the literatures which are time-saving and cost-saving compared with experimental-based research[21-23].

However, this numerical research did not take into account the intricate pore structure of metal foam, which hindered the exploration of the flow and heat transfer processes inside the pores. To overcome this limitation, the researches of the construction of geometric models for metal foam are conducted in the numerical simulations of flow and heat transfer. Pore-scale morphology of metal foam can be reconstructed using the micro-computed tomography (micro-CT) scan method [24, 25] or by generating an ideal cell geometry based on a virtual sample of regular polyhedrons. Dixit et al. [18] simulated the microstructure of metallic foams with a periodic structure of simple cubes. Yang et al. [26] simplified the structure of metal foam using the Weaire-Phelan structure. Corsini et al. [27] used a numerical algorithm to generate 3D, irregular open-pore porous structures synthetically, ensuring periodicity of the porous layer in all three directions. Furthermore, the tetrakaidecahedron structure is usually used as the approximate geometric cell of metal foam in the theoretical study of the various physical properties of metal foam [28-30].

Porosity and PPI are two critical parameters for describing the structure of metal foam. In this work, the tetrakaidecahedron cell structure is used to approximate the pore morphology of metal foam firstly, and then the hydraulic performance, thermal performance, and CHTP of HMF-filled heat sink with different porosity and PPI are numerically studied. Finally, GMF with graded direction and graded distribution are filled in the heat sinks to further improve the CHTP.

2. Geometric models of metal foam

2.1. Tetrakaidecahedron cell structure of metal foam

The structure of metal foam is based on the Kelvin cell, which forms due to the minimization of surface energy during the foam formation process. As the bubbles move freely in the melt, they

eventually form a unit cell structure with the smallest surface energy, which has a clear tetrakaidecahedron shape consisting of triangular prismatic ligaments and tetrahedron nodes. This structure is commonly observed in high-porosity metal foam, as shown in Fig. 1(a), and has been widely used as a structural model[31].

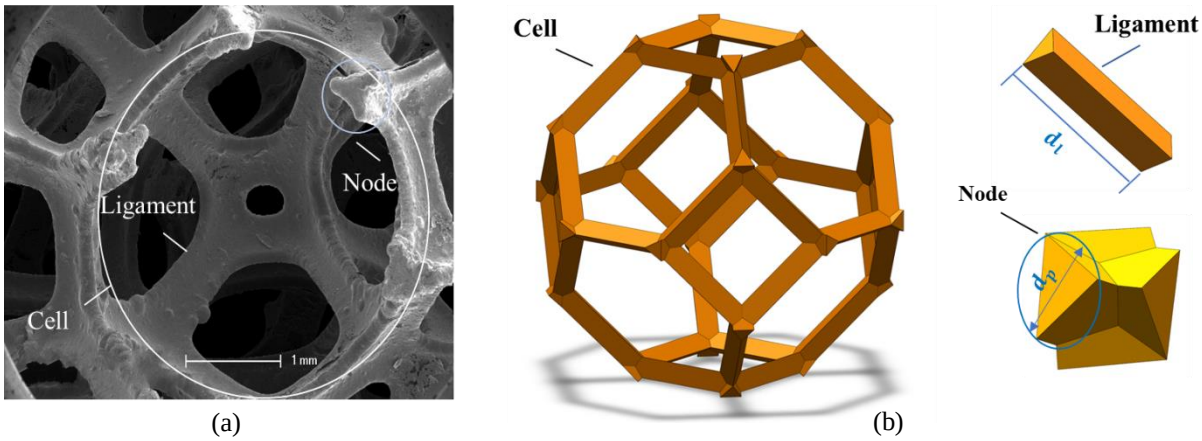

Fig. 1. Tetrakaidecahedron cell structure of metal foam: (a) SEM image and (b) 3D modeling models

Therefore, in this paper, 3D modeling software is used to create the shapes of three components,cell, ligament, and node, and they are developed the tetrakaidecahedron, triangular prism, and equivalent tetrahedron, respectively, as depicted in Fig. 1(b). Each tetrakaidecahedron consists of six squares and eight hexagons. The length of the triangular prism ligament is recorded as d_l, and the circumscribed circle diameter of the ligament cross-section is recorded as d_p.

2.2. Models of HMF and GMF

Porosity and PPI are two fundamental parameters that can be obtained with any metal foam[31-34], where the porosity can be defined by Eq.(1). The inscribed sphere diameter of each tetrakaidecahedron cell can be determined using Eq. (2), where PPI represents the number of pores per unit inch. The HMF with different porosity and PPI can be constructed by periodic arrays of tetrakaidecahedron with different sizes, as shown in Fig. 2.

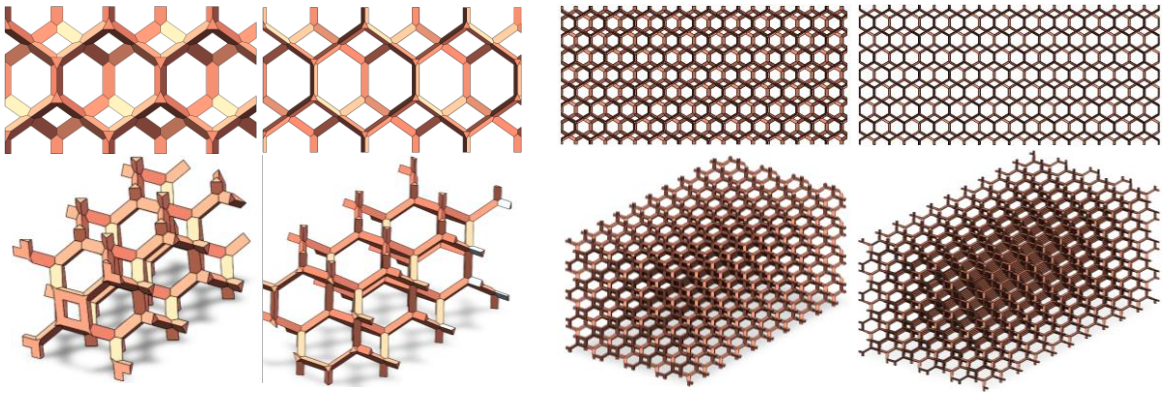

Fig. 2. Structures of HMF with different porosities and PPI

$$\varepsilon = \frac{V - V_f}{V} \tag{1}$$

where ε is the porosity. V and V_f are the overall volume and the solid phase volume of metal foam, respectively.

Assuming that each tetrakaidecahedron cell contains two pores in a certain direction when estimating PPI, then

$$d_r = \frac{2 \times 0.0254}{\mathrm{PPI}} \tag{2}$$

where d_r is the diameter of the inscribed sphere for a tetrakaidecahedron cell.

The simulation utilized the different synthetic structures with specific geometric parameters, which are listed in Tab. 1, where a_{sf} is the specific surface area. GMF can be constructed by combining HMF with different parameters. Parts of the structures of GMF used in this paper are shown in Fig. 3.

Table 1. Specific geometric parameters of different synthetic structures

PPI	Porosity	$d_r \times 10^{-3}$ m	$d_l \times 10^{-3}$ m	$d_p \times 10^{-3}$ m	a_{sf} m^{-1}
	0.950	10.16	2.18	1.49	255.34
5	0.965	10.16	2.39	1.22	225.36
	0.980	10.16	2.67	0.89	182.19
	0.950	5.08	1.09	0.74	505.22
10	0.965	5.08	1.20	0.61	440.84
	0.980	5.08	1.33	0.44	352.53
	0.950	2.54	0.55	0.37	1007.74
20	0.965	2.54	0.60	0.30	878.20
	0.980	2.54	0.67	0.22	695.52

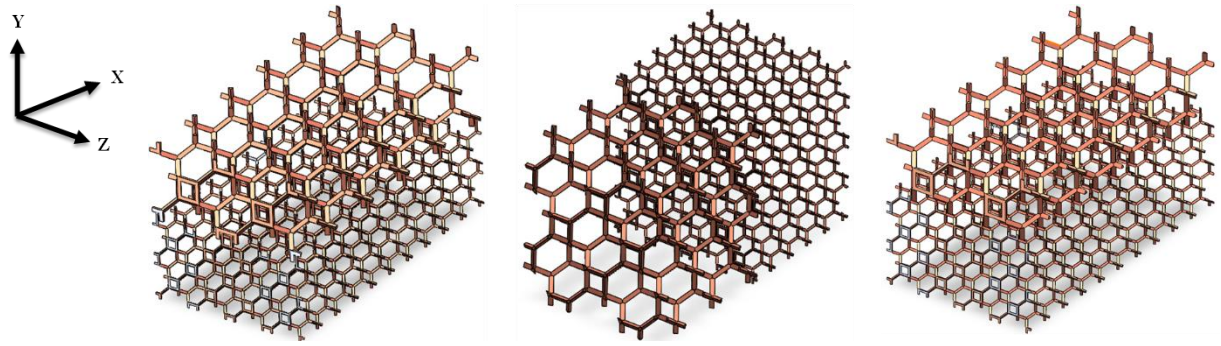

(a) Graded along the Y-axis (b) Graded along the X-axis (c) Graded along the Y-axis with different thickness

Fig. 3. Parts of the structures of GMF used in this paper

3. Mathematical modeling and numerical approach

3.1. Model description

This study involves the design and analysis of the 3D computational models of heat sinks filled with two types of metal foam, HMF and GMF. The numerical calculation model is represented by a schematic diagram in Fig. 4. The size of the fluid domain filled with metal foam is Lx=25.2mm, Ly=14.3mm, and Lz=14.3mm. The fluid computational domain is expanded by 15 mm both at the

front and rear, forming an extended calculation domain to eliminate the influence of the inlet and outlet.

The heat sink configurations in this study consist of two constrcutral types, HMF and GMF with different graded PPI which are graded in a stepwise manner either along the flow direction (X-axis direction) or perpendicular to the flow direction (Y-axis direction). Based on some references[11, 34], Tab. 2 shows the descriptions of the GMF-filled models used in present simulation study. The configurations of Cases 1, 2, 3, and 4 are designed to study the effect of graded PPI direction. Case 1 has a graded PPI from 10 to 20 (Positive change) along the Y-axis direction, and conversely, Case 2 has a graded PPI from 20 to 10 (Negative change) along the Y-axis direction. Comparing Case 1 and Case 2 can analyze the effect of different grade gradients along the Y-axis direction on heat dissipation. Case 3 has the graded PPI from 10 to 20 (Positive change) along the X-axis direction. In contrast, Case 4 has a graded PPI from 20 to 10 (Negative change) along the X-axis direction. Similarly, comparing Case 3 and 4 can analyze the effect of different grade gradients along the X-axis direction on heat dissipation. The configurations of Cases 5, 2, and 6 are designed to study the effect of graded PPI distribution. Both Cases 5, 2, and 6 have the grade PPI along the Y-axis direction, but they have different thicknesses. From Case 5 to Case 2, and Case 6, the thickness of PPI 20 gradually increases.

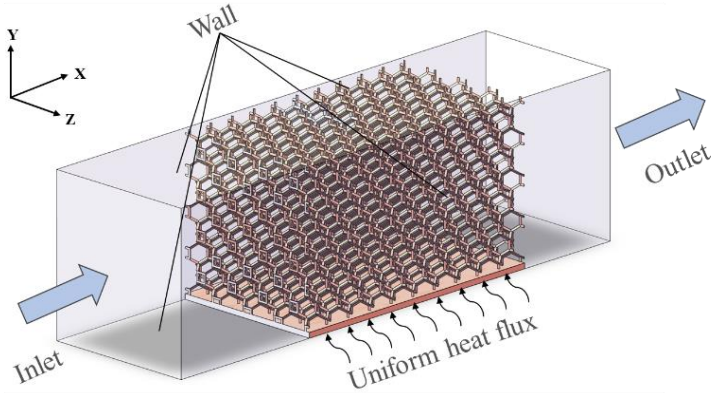

Fig. 4. Sketch map of the numerical calculation model

Table 2. GMF-filled heat sinks involved in the present study

	Model	Schematic diagrams of configurations
Grade PPI along the Y-axis direction	Case 1 (Positive Change)	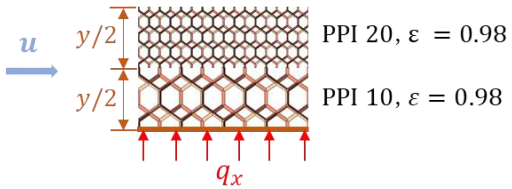
	Case 2 (Negative Change)	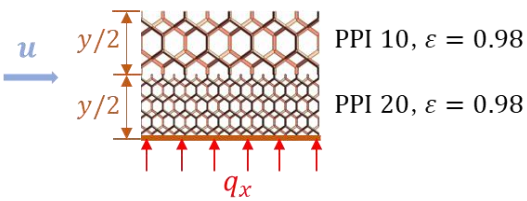

Grade PPI along the X-axis direction	Case 3 (Positive Change)	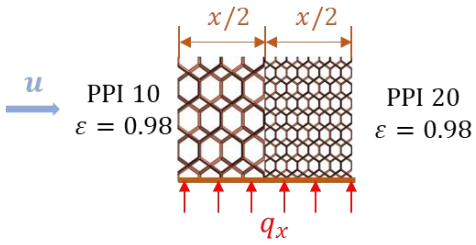
	Case 4 (Negative Change)	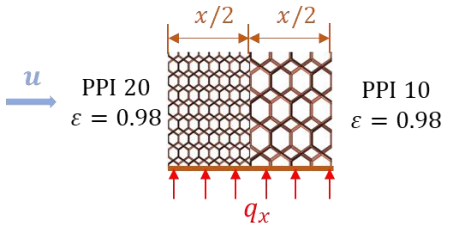
Grade PPI along the Y-axis direction with different thickness	Case 5	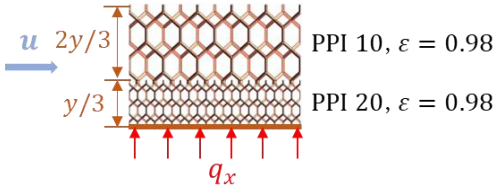
	Case 6	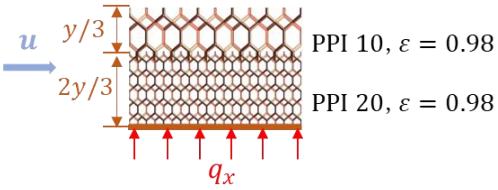

The air flows into the rectangular channel along the X-axis direction. A copper plate with 0.5mm thick is added on the heat source side to reduce contact thermal resistance. The heat sink is subjected to a uniform heat flux applied at the bottom. Initially, the heat is conducted from the bottom into the channel through a copper plate, and then dissipated through forced convection heat exchange between the air and the metal foam. Eventually, the heat is carried out of the heat dissipation channel along with the air. In order to simplify the computation, several assumptions are made: first, the metal foam is completely saturated with air and have isotropic properties. Second, heat radiation and gravity effects are ignored. Third, the air flow in the channel is stable and incompressible. Lastly, the porous structure does not deform with temperature changes.

The complex internal structure of the metal foam causes significant bending of the streamlines as air flows through it, resulting in separation and recirculation of the fluid. To account for this, the k-ε turbulence model based on the steady-state Navier-Stokes equation is utilized in the porous calculation area, as reported in previous studies equations describing the governing principles for the Newtonian fluid are presented as follows[25, 26, 35, 36].

Continuity equation:

$$\frac{\partial}{\partial x_i}(\rho u_i) = 0 \tag{3}$$

Momentum equation:

$$\frac{\partial}{\partial x_i}(\rho u_i u_j) = \frac{\partial}{\partial x_j}\left(\mu \frac{\partial u_i}{\partial x_j}\right) - \frac{\partial p}{\partial x_i} \tag{4}$$

Energy equation:

$$\frac{\partial}{\partial x_i}(\rho u_i T) = \frac{\partial}{\partial x_i}\left(\frac{\lambda}{c_p}\frac{\partial T}{\partial x_i}\right) \tag{5}$$

where p and ρ are the density and pressre, respectively; u, μ, c_p, λ, and T are the velocity, dynamic viscosity, specific heat capacity, thermal conductivity, and temperature, respectively.

Standard k-ε turbulence model equations[25, 26, 35]:

$$\rho \frac{\partial}{\partial x_i}(ku_i) = \frac{\partial}{\partial x_i}\left[\left(\mu + \frac{\mu_t}{\sigma_k}\right)\frac{\partial k}{\partial x_i}\right] + G_k - \rho\epsilon \tag{6}$$

$$\rho \frac{\partial}{\partial x_i}(\epsilon u_i) = \frac{\partial}{\partial x_j}\left[\left(\mu + \frac{\mu_t}{\sigma_\varepsilon}\right)\frac{\partial \epsilon}{\partial x_j}\right] + C_{1\varepsilon}\frac{\epsilon}{k}G_k - C_{2\varepsilon}\rho\frac{\epsilon^2}{k} \tag{7}$$

where $G_k = \mu_t \frac{\partial u_j}{\partial x_i}\left(\frac{\partial u_i}{\partial x_j} + \frac{\partial u_j}{\partial x_i}\right)$,the term μ_t represents the turbulent kinematic viscosity, that is $\mu_t = \rho C_\mu \frac{k^2}{\epsilon}$. $C_{1\epsilon}$, $C_{2\epsilon}$, and C_μ are all constants; σ_k is the turbulent Prandtl numbers for k and σ_ϵ is the turbulent Prandtl numbers for ϵ.

The heat transfer mechanism within the metal foam involves not only convective heat transfer between the solid skeleton and air, but also heat conduction between the connected solid skeletons. These mechanisms are not independent and are coupled through the governing equations that describe the fluid-solid coupling. In the calculations, air is considered as the fluid medium, while copper is used as the solid skeleton material for the metal foam. As the temperature range under investigation has little effect on physical parameters, constant physical properties are used for the calculations. Tab. 3 shows the physical parameters. The boundary conditions used in the calculations are listed below: (1) Inlet boundary: velocity inlet with a specified average velocity, inlet temperature 298 K. (2) Outlet boundary: pressure outlet with a set pressure of 0 Pa and the return temperature is 298 K. (3) Wall conditions: a constant heat flux of q_x = 50000 W/m^2 is applied on the bottom of the calculation domain filled with metal foam, and the remaining walls are set to insulated. (4) The walls where the fluid and solid frames are in contact are set as coupling walls.

Table 3. Physical parameters

Material	Density [kg/m^3]	Heat Capacity [J/(kg·K)]	Thermal conductivity [W/(m·K)]	Viscosity [kg/(m·s)]
Fluid material, air	1.225	1006.43	0.0242	1.7894×10^{-5}
Solid material, copper	8978	381	387.6	-

3.2. Numerical method and validation study

The numerical simulation of the flow and heat transfer process is conducted using FLUENT 14.0, which allows for the calculation of basic physical quantities such as velocity, temperature, and pressure in the flow field through computational fluid dynamics (CFD) calculations. The governing equations are discretized using the finite volume method, and the coupling of pressure and velocity is handled using the SIMPLE algorithm. The pressure term is discretized using the standard difference format, while the second-order upwind method is used for other terms during the difference process. In addition, to ensure the accuracy and reliability of the results, the convergence residuals of the energy equation and other variables were required to be less than 10^{-6}.

The hydraulic and heat transfer characteristics of metal foam are affected by the two parameters of porosity and PPI, which in turn affects the performance of the heat sink. Therefore, in order to maximize the performance of porous heat sinks, it is essential to achieve a balance between the

hydraulic and heat transfer characteristics. To achieve this, the dimensionless number pumping power $j/f^{1/3}$ is introduced as an evaluation index for the comprehensive hydraulic and heat transfer performance of heat sinks filled with different metal foam structures. The relevant parameters for this evaluation index are as follows[34].

$$Re = \frac{\rho u d_h}{\mu} \tag{8}$$

$$Nu = \frac{h d_h}{\lambda} \tag{9}$$

where d_h is the hydraulic diameter, which can be determined by Eq.(10) based on porous structure consideration; h is the convective heat transfer coefficient, which can be calculated by Eq.(11).

$$d_h = 4\frac{\varepsilon}{a_{sf}} \tag{10}$$

$$h = \frac{q_x}{\overline{T_s} - \overline{T_f}} \tag{11}$$

where $\overline{T_s}$ is the average temperature of the solid phase, and $\overline{T_f}$ is the average temperature of the fluid phase.

$$j = \frac{Nu}{Re \cdot Pr^{1/3}} \tag{12}$$

$$f = \frac{2\Delta p d_h}{\rho u^2} \tag{13}$$

where j is the heat transfer factor, and f is the resistance factor. Δp is the pressure drop between the inlet and outlet.

The geometric model is discretized using an unstructured grid consisting of tetrahedral elements. To ensure the accuracy of the numerical simulation results, the grid independence principle is employed to eliminate the influence of the number of grids on the calculation results. To assess the meshing grid independence, three different mesh quantities are tested: (1) 7 million, (2) 11 million, and (3) 15 million. The outlet average temperature of the heat sink is selected as the parameter for analysis, and the results indicate that there is a significant difference in the outlet average temperature between grid systems (1) and (2) at an inlet velocity of 2m/s, with a change of only 0.45%. However, under the same calculation conditions, the outlet average temperature of grid system (2) and (3) shows little difference, with a change of only 0.05%. This suggests that the simulation results are relatively independent of the grid quantity once a certain level of grid refinement has been achieved. Considering the balance between calculation time and calculation accuracy, the grid division of the model selects the grid system (2) with a grid number of 11 million.

Fig. 5 illustrates a comparison between the convective heat transfer coefficient obtained from numerical simulation and the existing experimental results to validate the accuracy of the numerical results. The simulation is conducted with adiabatic boundary conditions, and the temperature of the metal foam is set to 298 K. The results indicate a good agreement between the heat transfer coefficients obtained from the simulation and those reported by Diani et al.[37] and Mancin et al.[38], with a relative root-mean-square error (RRMSE) less than 7%. As such, the numerical simulation model can be considered reliable for subsequent calculations. The RRMSE serves as an estimate of the error between the numerical and experimental data[39].

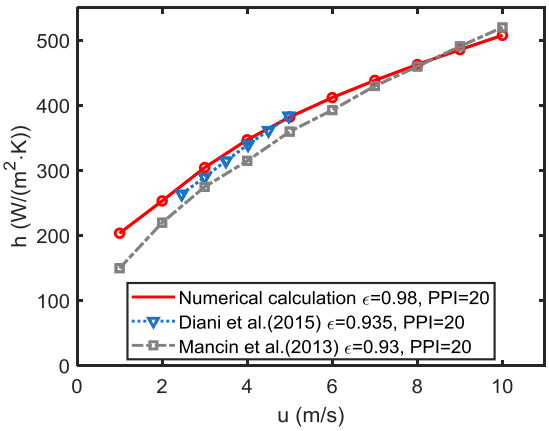

Fig. 5. Comparison of the convective heat transfer coefficient between simulation and experiment

4. Results and discussion

4.1. Hydraulic performance of HMF-filled heat sinks

Fig. 6 shows the pressure drops of the HMF-filled heat sinks configurations with different porosities and PPI under different flow rates. It can be found the unit pressure drop of metal foam exhibits an almost power function growth trend with increasing fluid flow rate. As porosity increases, the pressure drop decreases gradually. This is primarily due to the fact that higher porosity results in better permeability of the metal foam, reduced obstruction in the flow channel, easier fluid passage, and smaller resistance coefficient. Conversely, as PPI increases, the pressure drop increases gradually. This is because higher PPI leads to smaller pore diameter of metal foam, lower permeability, and greater flow resistance. Under the same porosity, the unit pressure drop of PPI20 is 3-5 times that of PPI5. When the fluid velocity is 2 m/s, the unit pressure drop of PPI10 is 0.67 kPa·m^{-1} larger than that of PPI5, and that of PPI20 is 1.34 kPa·m^{-1} larger than that of PPI10 under the same porosity of 0.95. However, at 10 m/s, the unit pressure drop of PPI10 is 18.93 kPa·m^{-1} larger than that of PPI5, and that of PPI20 is 35.12 kPa·m^{-1} larger than that of PPI10. It can be inferred that as the flow rate increases, the gap between the unit pressure drops of different pore densities increases.

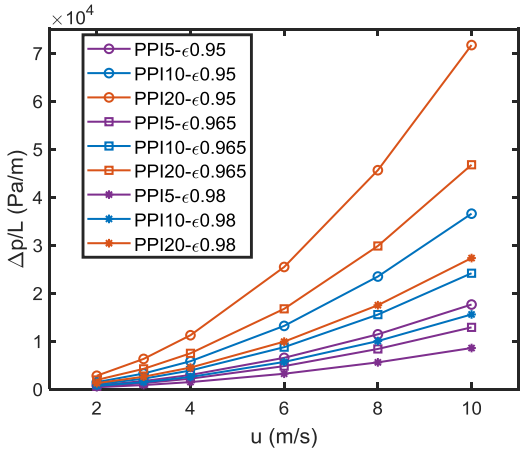

Fig. 6. The pressure drops of different HMF-filled heat sinks

Due to this difference, when designing metal foam heat sinks, it is necessary to consider the convective heat transfer of flow rate, so it is very important to summarize the resistance characteristic formula of metal foam at different flow rates under the influence of PPI and porosity. As mentioned

above, there is a power function relationship between unit pressure drop and flow rate, so the fitting formulae can be obtained by the form of $\Delta p/L = C\,u^{1.9}$, as shown in Tab. 4. The R-square error of each fitting formula is greater than 0.999. Parameter C is dependent on both PPI and porosity, and it increases with an increase in PPI and a decrease in porosity. Therefore, the parameter C can be expressed as a function of $\varepsilon^{-\mathrm{PPI}}$, and the fitting formula of the hydraulic performance can be obtained by fitting by the least square method as follow.

$$\frac{\Delta p}{L} = (6.45\varepsilon^{-3\mathrm{PPI}} - 131.3\varepsilon^{-2\mathrm{PPI}} + 889.3\varepsilon^{-\mathrm{PPI}} - 719.6)u^{1.9} \tag{14}$$

Table 4. Pressure drops fitting formulae under different PPI and porosity

PPI \ Porosity	0.95	0.965	0.98
5	$\frac{\Delta p}{L} = 220.1u^{1.9}$	$\frac{\Delta p}{L} = 160.9u^{1.9}$	$\frac{\Delta p}{L} = 107.0u^{1.9}$
10	$\frac{\Delta p}{L} = 454.0u^{1.9}$	$\frac{\Delta p}{L} = 300.2u^{1.9}$	$\frac{\Delta p}{L} = 193.5u^{1.9}$
20	$\frac{\Delta p}{L} = 887.4u^{1.9}$	$\frac{\Delta p}{L} = 579.7u^{1.9}$	$\frac{\Delta p}{L} = 339.4u^{1.9}$

The flow rate, porosity, and PPI applicable scopes of this fitting formula are 1m/s to 10m/s, 0.9 to 0.99, and 5 to 20, respectively. In order to assess the accuracy and validity of the formula, classical experimental data at different PPI and porosity values under varying flow rates are selected for comparison, as illustrated in Fig. 7. The comparison revealed good agreement between the model data and the experimental data when the flow rate is less than 5m/s. However, at higher flow rates, the error increased. The error between the model results and the experimental data is quantified using RRMSE, the RRMSE values of PPI10 and ε=0.9, PPI20 and ε=0.9, PPI20 and ε=0.93 are 15.0%, 14.3%, and 18.8%, respectively, when compared with the experimental data reported in previous studies[40-43].

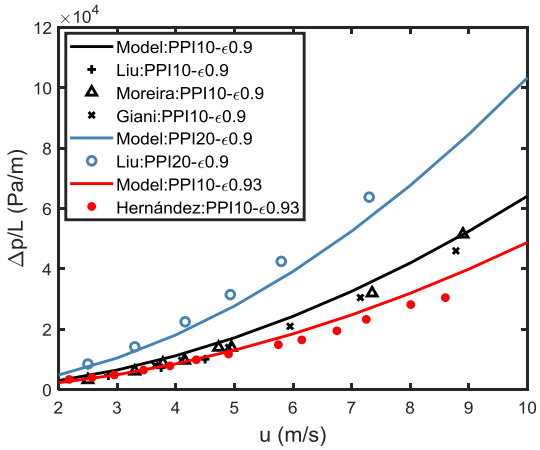

Fig. 7. Comparison of pressure drops between the model in this paper and the experimental data in literature

4.2. Thermal performance of HMF-filled heat sinks

Fig. 8 displays the CHTP of different HMF-filled heat sink configurations with varying porosities and PPI under diverse flow rates. The results indicate that as the PPI increases and the porosity decreases, there is a gradual increase in pressure drop, while the CHTP also improves progressively. When the PPI remains constant, the CHTP exhibits a gradual increase with a decrease in porosity. Conversely, when the porosity is constant, the CHTP gradually increases with an increase in PPI.

These observations can be attributed to two factors. Firstly, a smaller porosity results in a larger ligament diameter when the PPI is constant. Secondly, when the porosity is constant, a larger PPI leads to a smaller equivalent diameter of the tetrakaidecahedron cell. Both of these factors contribute to an increase in the specific surface area, which ultimately enhances heat transfer between the fluid and the solid. It is evident that the CHTP of metal foam is positively correlated with the specific surface area of the metal foam, and the trend in heat transfer performance under different porosity and PPI changes is consistent with the trend in specific surface area.

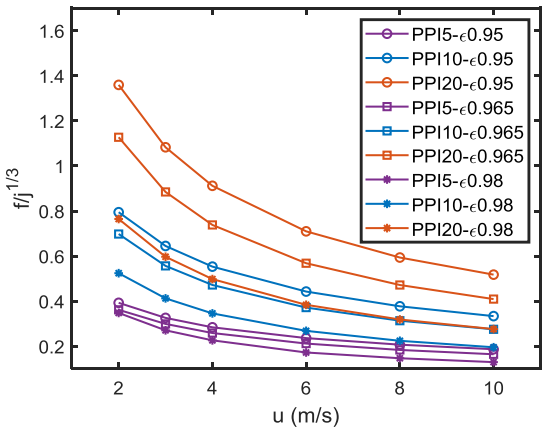

Fig. 8. The CHTP of the heat sink filled in HMF

To facilitate the prediction of heat transfer performance in HMF-filled heat sinks based on PPI and porosity, it is essential to establish a correlation formula for convective heat transfer. In the convective heat transfer studies, characteristic numbers with dimension one, such as Re, Pr, and Nu, are commonly used to express various physical quantities involved in the heat transfer process. The correlation formula for forced convective heat transfer in a rectangular channel can be expressed as a power function of these characteristic numbers[44].

$$Nu = CRe^{n}Pr^{w} \tag{15}$$

For a clear understanding of this equation, the values of Nu at different Re are obtained using Eqs. (8) and (9), and then the fitting of the correlation formula is completed. In this study, the Pr value is considered constant at 0.7, as its change is not significant within a certain temperature range. The correlation formula for forced convective heat transfer in porous media includes a constant *C*, which can range from 0.3 to 0.6, and a constant *w* with the value of 1/3[45]. The linear equation can be obtained as shown in Eq. (18) by taking the logarithm on both sides of Eq. (17).

$$\ln Nu = n\ln Re + \ln C + \frac{1}{3}\ln Pr \tag{16}$$

Therefore, the slope of the linear equation is *n*, and the intercept is $\ln C + \frac{1}{3}\ln Pr$. The coefficients *C* and *n* can be obtained by using the least squares method. Once the values of *C* and *n* have been obtained, the convective heat transfer correlation formula can be fitted. Tab. 5 shows the fitting correlation formulae under different porosities.

Table 5. Convective heat transfer correlation formulae under different porosity

Porosity	Straight lines of fitting	Empirical formulae
0.950	$\ln Nu = 0.37 \ln Re + 4.567$	$Nu = 108.407\, Re^{0.37} Pr^{1/3}$
0.965	$\ln Nu = 0.37 \ln Re + 4.422$	$Nu = 93.774\, Re^{0.37} Pr^{1/3}$
0.980	$\ln Nu = 0.37 \ln Re + 4.212$	$Nu = 76.012\, Re^{0.37} Pr^{1/3}$

It reveals that the coefficient C increases gradually with an increase in porosity. It shows that as the porosity increases, the Nu gradually becomes smaller, indicating that convective heat transfer weakens gradually. As the porosity increases, the volume proportion of filled metal foam decreases, thereby reducing the efficiency of heat conduction from the heat source. Therefore, the coefficient C can be expressed as a quadratic polynomial function of porosity, and the convective heat transfer correlation formula can be obtained as follows.

$$Nu = (-6953.3\varepsilon^2 + 12340\varepsilon - 5339.3)\, Re^{0.37} Pr^{1/3} \tag{17}$$

To validate the correctness and accuracy of the formula, a case study of PPI15 and ε=0.98 is conducted. The results, as shown in Fig. 9, demonstrate that the relationship between Re and Nu calculated by the model is in excellent agreement with the validation data, with a RRMSE of only 0.8%.

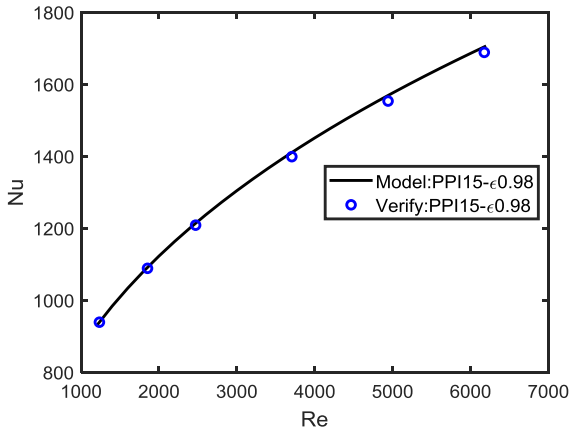

Fig. 9. Validation of heat transfer empirical formula for the HMF-filled heat sinks

4.3. CHTP of GMF-filled heat sinks

4.3.1 Effect of graded PPI direction

The graded PPI of the metal foam in Case 3 and 4 are along the fluid flow direction (X-axis direction), where the PPI of Case 3 gradually increases from 10 to 20 (positive change), and the PPI of Case 4 gradually decreases from 20 to 10 (negative change). Fig. 10(a) shows the a comparison of the CHTP between Case 3, Case 4, and HMF of PPI 10, PPI 15, and PPI 20. It is observed that the CHTP of Case 3 and 4 in the positive and negative changes along the X-axis direction are nearly identical, with only slight difference at lower flow rates. Moreover, the CHTP of Case 3 and Case 4 is between the CHTP of HMF with PPI 10 and PPI 20, and better than the CHTP of HMF with PPI 15. This illustrates that under the condition of equal average PPI, graded PPI along the X-axis direction can improve CHTP, and the graded PPI changes in either positive or negative directions have the same effect.

The graded PPI of the metal foam in Case 1 and 2 are along the direction perpendicular to the fluid flow (Y-axis direction), where the PPI of Case 1 gradually increases from 10 to 20 (Positive change), and the PPI of Case 2 gradually decreases from 20 to 10 (Negative change). Fig. 10(b) displays a comparison of the CHTP between Case 1, Case 2, and HMFs of PPI 10, PPI 15, and PPI 20. It is evident that the CHTP of Case 1 and 2 lies between the HMF with PPI10 and PPI20, but the CHTP of Case 2 is significantly greater than that of Case 1. Furthermore, the CHTP of Case 2 is greater than that of HMF with PPI 15 and the CHTP of Case 1 is less than that of HMF with PPI 15. This illustrates that under the condition of equal average PPI, graded PPI negative change along the Y-axis direction can greatly improve CHTP, but it is worth noting that the positive change in graded PPI along the Y-axis direction has no impact on improving CHTP.

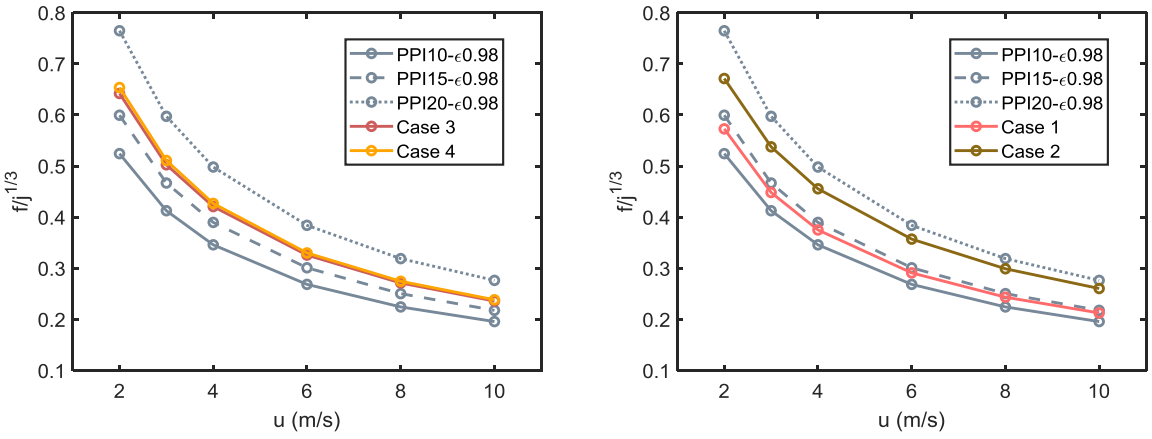

(a) (b)

Fig. 10. Comparison of the CHTP: (a) between Case 3 and Case 4; (b) between Case 1 and Case 2

To summarize, the GMF-filled heat sink with graded PPI can enhance CHTP in comparison to the HMF-filled heat sink. When it comes to graded PPI along the Y-axis direction, the negative change in graded PPI produces a better improvement in CHTP than the positive change. However, the positive change or negative change of the graded PPI along the X-axis direction has an equal effect. Among the GMF-filled heat sinks of Case 1, 2, 3, and 4, Case 2 exhibits the highest CHTP.

4.3.2 Effect of graded PPI distribution

Based on the research conclusions in Section 4.3.1, Case 2 where the PPI 20 metal foam is placed close to the heat source and the graded PPI decreases along the Y-axis direction has the better CHTP. To further understand the temperature distribution of GMF-filled heat sinks, the configurations of the different thicknesses of PPI 20 named Case 5, Case 2, and Case 6, respectively, are comparatively studied. From Case 5 to Case 2, and Case 6, the thickness of PPI 20 metal foam gradually increases. The CHTP of Case 5, 2, and 6 are shown in Fig. 11. It is observed that the CHTP improves with an increase in the thickness of PPI 20.

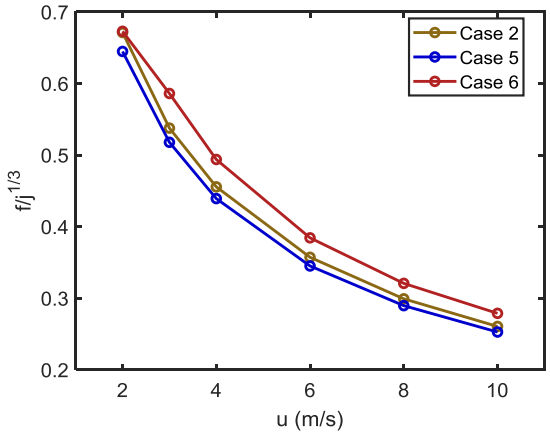

Fig. 11. Comparison of the CHTP for Case 5, 2, and 6

The temperature fields of the bottom plane and central x-y cross-section of Case 5, 2, and 6 are shown in Fig. 12. It can be seen that a negative change in graded PPI along the Y-axis direction can significantly change the temperature distribution of the bottom plane and reduce the maximum temperature. Additionally, an increase in the thickness of PPI 20 results in a decrease in the maximum temperature of the bottom surface and an improvement in the uniformity of the temperature field. This is due to the fact that the interior of the metal foam involves not only convective heat transfer between the solid frames and the air, but also heat conduction from the heat source along the solid skeleton. The heat applied at the bottom plane is initially released through heat conduction of the solid skeleton and then dissipated through forced convective heat transfer between the coolant and the solid skeleton. Finally, the heat is carried out of the heat dissipation channel along with the air. Increasing the thickness of PPI 20 closer to the heat source enhances the heat conduction along the solid frame and forced convective heat transfer between the air and the solid frame, leading to a decrease in the maximum temperature of the bottom surface and an improvement in the uniformity of the temperature field.

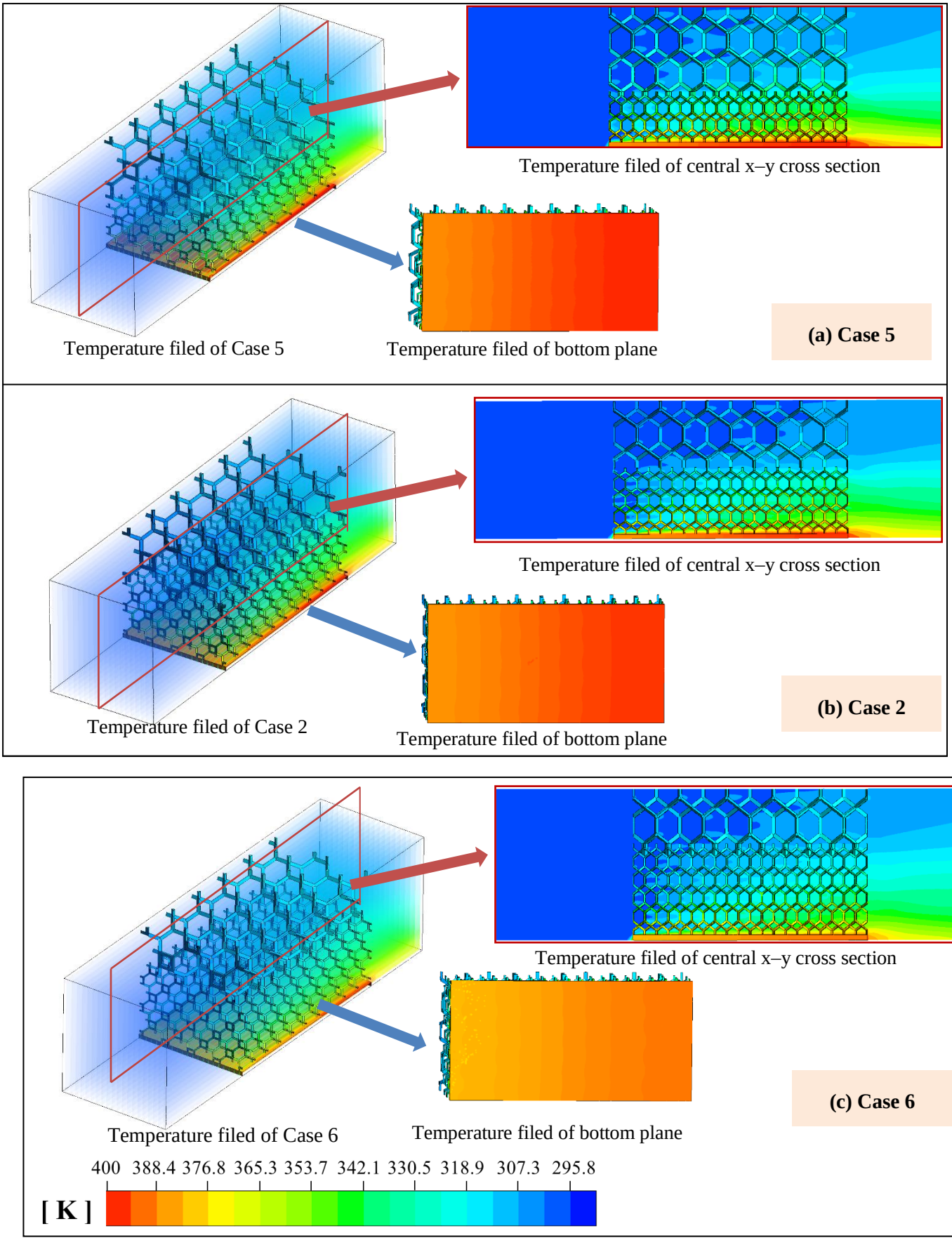

Fig. 12. Temperature fields of the bottom plane and central x–y cross-section of Case 5, Case 2, and Case 6

5. Conclusion

In this study, the 3D tetrakaidecahedron topology structure of the metal foam is constructed. The computational fluid dynamics method is used to numerically study the hydraulic performance and heat transfer performance of HMF-filled heat sinks with different porosities and PPI, and the corresponding empirical relational formulae are obtained. Moreover, the CHTP of GMF-filled heat sinks with different graded PPI directions and distribution are studied. Results show that the reasonable design of the GMF-filled heat sink with graded PPI can effectively improve CHTP. The graded PPI change along the X-axis direction can improve the CHTP, and whether the positive or negative change has the same effect. The graded PPI negative change along the Y-axis direction can efficiently improve the CHTP, and the greater the thickness of the metal foam with larger PPI the better the performance, but positive change has no effect. In addition, the GMF-filled heat sink can effectively suppress the surface temperature of the bottom plane heat source. It can reduce the maximum temperature on the bottom plane and significantly homogenizes the temperature field. The findings reported in present work provide an effective method to improve the CHTP of GMF-filled heat sinks by changing the configurations of graded PPI.

References

[1] Thiangchanta, S., et al., Energy reduction for commercial freezer by force convection cooling of heatsink, *Energy Reports*, 8. (2022), pp. 394-399.

[2] Fu, J.H., et al., Enhanced heat transfer research in liquid-cooled channel based on piezoelectric vibrating cantilever, *Thermal Science*, 25. (2021), 2, pp. 823-832.

[3] Zheng, M., et al., Numerical study on power battery thermal management system based on heat pipe technology, *Energy Reports*, 9. (2023), pp. 350-361.

[4] Zhao, J., et al., Thermal management strategy for electronic chips based on combination of a flat-plate heat pipe and spray cooling, *International Journal of Heat and Mass Transfer*, 181. (2021), pp. 121894

[5] Wang, B.C., et al., Development and numerical investigation of novel gradient-porous heat sinks, *Energy Conversion and Management*, 106. (2015), pp. 1370-1378.

[6] Wang, X.X.,F. Lin, Numerical analysis on heat transfer and flow resistance performances of a heat exchanger with novel perforated wavy fins, *Thermal Science*, 26. (2022), 4B, pp. 3345-3357.

[7] Abdelmohimen, M.A.H., et al., Numerical investigationof using different arrangement of fin slides on the plate-fin heat sink performance, *Thermal Science*, 25. (2021), 6, pp. 4683-4693.

[8] Fathi, M., et al., Porous-fin microchannel heat sinks for future micro-electronics cooling, *International Journal of Heat and Mass Transfer*, 202. (2023), pp. 123662

[9] Jin, Q., et al., Oscillatory valve effect on pressure drop oscillation in microchannel cooling system, *International Journal of Heat and Mass Transfer*, 206. (2023), pp. 123931.

[10] Samudre, P.,S.V. Kailas, Thermal performance enhancement in open-pore metal foam and foam-fin heat sinks for electronics cooling, *Applied Thermal Engineering*, 205. (2022), pp. 117885.

[11] Marri, G.K.,C. Balaji, Experimental and numerical investigations on the effect of porosity and PPI gradients of metal foams on the thermal performance of a composite phase change material heat sink, *International Journal of Heat and Mass Transfer*, 164. (2021), pp. 120454.

[12] Bianco, N., et al., Multi-objective optimization of finned metal foam heat sinks: Tradeoff between heat transfer and pressure drop, *Applied Thermal Engineering*, 182. (2021), pp. 116058.

[13] Wan, T., et al., Fabrication, properties, and applications of open-cell aluminum foams: A review, *Journal of Materials Science & Technology*, 62. (2021), pp. 11-24.

[14] Cui, W., et al., Heat transfer enhancement of phase change materials embedded with metal foam for thermal energy storage: A review, *Renewable & Sustainable Energy Reviews*, 169. (2022), pp. 112912.

[15] Kundu, P.K., *et al.*, Flow features of a conducting fluid near an accelerated vertical plate in porous medium with ramped wall temperature, *Journal of Mechanics*, *30*. (2014), 03, pp. 277-288.
[16] Das, K., Forced convective flow over a porous plate with variable fluid properties and chemical reaction: an application of the lie group transformation, *Moldavian Journal of the Physical Sciences*, 16. (2017), pp. 46-63.
[17] Das, K., *et al.*, Investigation of the effects of different models of nanofluids on their flow and heat transfer characteristics, *Journal of the Korean Physical Society*, 67. (2015), 7, pp. 1167-1174.
[18] Dixit, T.,I. Ghosh, An experimental study on open cell metal foam as extended heat transfer surface, *Experimental Thermal and Fluid Science*, *77*. (2016), pp. 28-37.
[19] Zhong, Z.D., *et al.*, Enhanced heat transfer performance of optimized micro-channel heat sink via forced convection in cooling metal foam attached on copper plate, *Journal of Energy Storage*, *30*. (2020), pp. 101501.
[20] Lotfizadeh, H., *et al.*, Thermal performance of an innovative heat sink using metallic foams and aluminum nanoparticles-Experimental study, *International Communications in Heat and Mass Transfer*, *66*. (2015), pp. 226-232.
[21] Li, Y.T., *et al.*, Hydraulic and thermal performances of metal foam and pin fin hybrid heat sink, *Applied Thermal Engineering*, *166*. (2020), pp. 114665.
[22] Li, Y.T., *et al.*, Thermal Performance of Metal Foam Heat Sink With Pin Fins for Nonuniform Heat Flux Electronics Cooling, *Journal of Electronic Packaging*, *143*. (2021), 1, pp. 011006.
[23] Sahin, Y.S., *et al.*, Investigation of flow and heat transfer behavior of integrated pin fin-aluminum foam heat sink, *Applied Thermal Engineering*, *219*. (2023), pp. 119504.
[24] Hamidi, E., *et al.*, Lattice Boltzmann Method simulation of flow and forced convective heat transfer on 3D micro X-ray tomography of metal foam heat sink, *International Journal of Thermal Sciences*, *172*. (2022), pp. 107240.
[25] Yu, P.X., *et al.*, Pore-scale numerical study of flow characteristics in anisotropic metal foam with actual skeleton structure, *International Communications in Heat and Mass Transfer*, *126*. (2021), pp. 105401.
[26] Yang, K., *et al.*, Pore-scale numerical simulation of convection heat transfer in high porosity open-cell metal foam under rotating conditions, *Applied Thermal Engineering*, *195*. (2021), pp. 117168.
[27] Corsini, R.,E. Stalio, Direct numerical simulation of turbulence in the wake of a metal foam, *International Communications in Heat and Mass Transfer*, *115*. (2020), pp. 104599.
[28] Zhang, C., *et al.*, A Predicting Model for the Effective Thermal Conductivity of Anisotropic Open-Cell Foam, *Energies*, *15*. (2022), 16, pp. 6091.
[29] Yang, H.Z., *et al.*, Effective thermal conductivity of high porosity open-cell metal foams, *International Journal of Heat and Mass Transfer*, *147*. (2020), pp. 118974.
[30] Chen, J., *et al.*, Calculation Method of Specific Surface Area of Foam Metal Based on an Ideal Tetradecahedron Model for Lithium Ion Battery, *International Journal of Photoenergy*, *2020*. (2020), pp. 2478579.
[31] Kanaun, S.,E. Tkachenko, Effective conductive properties of open-cell foams, *International Journal of Engineering Science*, *46*. (2008), 6, pp. 551-571.
[32] Shen, H., *et al.*, The simplified analytical models for evaluating the heat transfer performance of high-porosity metal foams, *International Journal of Thermophysics*, *39*. (2018), 7, pp. 87
[33] Thomson, W., On the division of space with minimum partitional area, *Acta mathematica*, *11*. (1887), 1, pp. 121-134
[34] Jadhav, P.H., *et al.*, Analysis of functionally graded metal foams for the accomplishment of heat transfer enhancement under partially filled condition in a heat exchanger, *Energy*, *263*. (2023), pp. 125691.
[35] Jadhav, P.H., *et al.*, Performance evaluation of partially filled high porosity metal foam configurations in a pipe, *Applied Thermal Engineering*, *194*. (2021), pp. 117081.
[36] Das, K., *et al.*, Magneto chemically reacting micropolar nanofluid flow in existence of heat source/sink, *Journal of Nanofluids*, *11*. (2022), 4, pp. 528-536.
[37] Diani, A., *et al.*, Numerical investigation of pressure drop and heat transfer through reconstructed metal foams and comparison against experiments, *International Journal of Heat and Mass Transfer*, *88*. (2015), pp. 508-515.

[38] Mancin, S., *et al.*, Air forced convection through metal foams: Experimental results and modeling, *International Journal of Heat and Mass Transfer*, *62*. (2013), pp. 112-123.
[39] Shen, H., *et al.*, Modeling and simulation of the discharge process of isothermal chamber to determine the isothermal characteristic, *Journal of Thermal Science and Technology*, *17*. (2022), 1, pp. 00353.
[40] Liu, H., *et al.*, Simulation and analytical validation of forced convection inside open cell metal foams, *International Journal of Thermal Sciences*, *111*. (2017), pp. 234-245.
[41] Moreira, E.A., *et al.*, Permeability of ceramic foams to compressible and incompressible flow, *Journal of the European Ceramic Society*, *24*. (2004), 10-11, pp. 3209-3218.
[42] Giani, L., *et al.*, Mass-transfer characterization of metallic foams as supports for structured catalysts, *Industrial & Engineering Chemistry Research*, *44*. (2005), 14, pp. 4993-5002.
[43] Hernández, Á., Combined flow and heat transfer characterization of open cell aluminum foams, University of Puerto Rico,2005.
[44] Yang, L., *et al.*, Experimental study of the convection heat transfer model of porous media for isothermal chamber during discharging, *Experimental Thermal and Fluid Science*, *61*. (2015), pp. 87-95.
[45] Zheng, K.C., *et al.*, Review on forced convection heat transfer in porous media, *Acta Physica Sinica*, *61*. (2012), 1, pp. 532-542.

Paper submitted: 25.07.2023
Paper revised: 20.09.2023
Paper accepted: 26.09.2023